High Resolution Simulation of Beam Dynamics in Electron Linacs for Free Electron Lasers

J. Qiang, R. D. Ryne, M. Venturini, A. A. Zholents

Lawrence Berkeley National Laboratory,

Berkeley, CA 94720

I. V. Pogorelov

Tech-X Corporation, Boulder, CO 80303

In this paper we report on large scale multi-physics simulation of beam dynamics in electron linacs for next generation free electron lasers (FELs). We describe key features of a parallel macroparticle simulation code including three-dimensional (3D) space-charge effects, short-range structure wake fields, longitudinal coherent synchrotron radiation (CSR) wake fields, and treatment of radio-frequency (RF) accelerating cavities using maps obtained from axial field profiles. A macroparticle up-sampling scheme is described that reduces the shot noise from an initial distribution with a smaller number of macroparticles while maintaining the global properties of the original distribution. We present a study of the microbunching instability which is a critical issue for future FELs due to its impact on beam quality at the end of the linac. Using parameters of a planned FEL linac at Lawrence Berkeley National Laboratory (LBNL), we show that a large number of macroparticles (beyond 100 million) is needed to control numerical shot noise that drives the microbunching instability. We also explore the effect of the longitudinal grid on simulation results. We show that acceptable results are obtained with around 2048 longitudinal grid points, and we discuss this in view of the spectral growth rate predicted from linear theory. As an application, we present results from simulations using one billion macroparticles of the FEL linac under design at LBNL. We show that the final uncorrelated energy spread of the beam depends not only on the initial uncorrelated energy spread but also depends strongly on the shape of the initial current profile. By using a parabolic initial current profile, 5 keV initial uncorrelated energy spread at 40 MeV injection energy, and improved linac design, those simulations demonstrate that a reasonable beam quality can be achieved at the end of the linac, with the final distribution having about 100 keV energy spread, 2.4 GeV energy, and 1.2 kA

peak current.

I. INTRODUCTION

The electron beam quality at the entrance of an undulator will have a significant impact on the performance of the next generation FELs. In order to achieve good performance in the x-rays output at a reasonable cost, the emittance and energy spread of the electron beam are required to meet tight specifications while allowing for a fairly high peak current. However, collective effects such as the microbunching instability driven by space-charge, structure wake fields, and CSR can cause an unacceptable degradation of beam quality [1–4] and pose a challenge both in terms of beam dynamics modelling and machine design optimization. Previous studies have shown that small density fluctuations in an electron beam can lead to significant growth of energy fluctuations through a linac as a result of longitudinal space charge. After passing through a bunch compressor, energy fluctuations are converted into density modulations and are further amplified in the presence of CSR. This phenomenon, the so-called 'microbunching instability' results in the growth of the uncorrelated energy spread, the appearance of large current fluctuations, and a general degradation of beam quality. The gain of the instability can be large enough to amplify to unacceptable level the small density fluctuations due to shot noise [5].

The microbunching instability has been studied using both microparticle tracking [6] and a direct Vlasov solver [7]. Direct Vlasov solvers do not suffer from the numerical sampling noise characteristic of macroparticle sampling and may provide an accurate description of the microbunching instability both in the linear and nonlinear regimes. However, in the implementation presently available this method is limited to a simplified two-dimensional phase-space computational model with collective effects treated in the mean-field approximation.

Macroparticles codes provide well established and successful methods for studying beam dynamics but they tend to overestimate the effect of instabilities that are sensitive to small fluctuations of the beam density, like those generated by shot noise. These will be magnified by a factor $\sqrt{N_{\rm mp}/N}$ in a simulation employing $N_{\rm mp}$ macroparticles to represent a beam of N electrons.

The tracking code ELEGANT (in which all collective effects including longitudinal space charge are modelled in terms of wake potentials) has been successfully used to simulate the microbunching instability in the linear regime using a number of macroparticles significantly smaller (up to $N_{\rm mp} =$ 60M) than the bunch population by a judicious use of low-pass filters [6]. However, tuning the

filters properly beyond the linear regime, where guidance from linear theory may be lost, can be problematic.

A more straightforward and robust path toward increasing the accuracy of the simulations is to employ a larger number of macroparticles. Progress in the availability of high power computational resources and program design have made it possible to pursue this path in the development of the parallel code IMPACT, making it practical to carry out simulations with a one billion (1B) or more macroparticles (a number comparable to a typical electron bunch population). IMPACT models space-charge forces (the main drive of the microbunching instability) in the full three-dimensional (3D) configuration space by numerical solution of the Poisson equation, which is needed to guarantee good accuracy. The code is now being extensively used in design studies for a proposed 4th generation light source at LBNL.

As an illustration of the relevance of the microbunching instability and the importance of using a large population of macroparticles in the simulations, we present here a case study summarized in Figure 1. This is an example of longitudinal phase space distribution at the end of the linac for the x-ray FEL at FERMI@ELETTRA [8]. The charge of the electron bunch is 0.8 nC. The final designed peak current is about 800 A with an energy of 1.2 GeV. The picture contains the superposition of the results of three distinct simulations for a beam with $N = 5$ billion electrons/bunch. In the first simulation (blue points) the beam was propagated through the linac with space-charge and coherent synchrotron radiation (CSR) wakes turned off. In the second and third simulation the space charge and CSR were turned on using 10M (red points) and 1B (green points) macroparticles per bunch. In the absence of collective effects the final longitudinal distribution has a smooth shape with a fairly small energy spread. It is clear from the picture that including space-charge and CSR effects significantly degrades the beam quality and yields a much larger uncorrelated spread and phase space modulations. Moreover, it is also evident that the simulation carried out with a larger number of macroparticles shows modulations of significantly smaller amplitude.

The purpose of the present paper is to report on the latest developments in the code IMPACT that have made possible these simulations while providing a discussion of the need for large scale multi-physics simulations. The organization of this paper is as follows: the computational model used in the beam dynamics simulation is presented in section 2; the choice of numerical parameters is discussed in section 3; large scale simulation of the planned LBNL FEL linac is presented in section 4; and the summary is given in section 5.

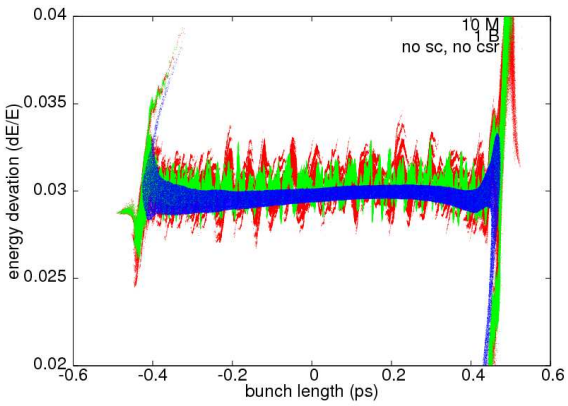

FIG. 1: Longitudinal phase space distribution at the end of the linac from simulations using 10 million and one billion macroparticles together with the case without space-charge and CSR effects.

II. COMPUTATIONAL MODEL

The beam dynamics simulation of the FEL linac was performed using a parallel macroparticle tracking code, IMPACT [9]. The IMPACT code is an object-based parallel particle-in-cell code to simulate high intensity, high brightness beam transport mainly in RF linear accelerators. It uses a split-operator method to separate the particle advance subject to the given external fields from the particle advance subject to the collective self-consistent space-charge fields or wake fields [10].

A. Modelling of RF Structures

Beam dynamics inside an RF cavity, including longitudinal accelerating fields and transverse focusing fields, is modeled using linear transfer maps and multiple reference particles along the bunch. The vector potentials associated with an axis-symmetric RF cavity, specified through the order needed to compute linear dynamics, are

$$A_x = \frac{\varepsilon'(z)}{2\omega_\alpha} x \sin(\omega_\alpha t + \theta) \tag{1}$$

$$A_y = \frac{\varepsilon'(z)}{2\omega_\alpha} y \sin(\omega_\alpha t + \theta) \tag{2}$$

$$A_z = -\frac{1}{\omega_\alpha}(\varepsilon(z) - \frac{r^2}{4}[\varepsilon''(z) + \frac{\omega_\alpha^2}{c^2}\varepsilon(z)]) \sin(\omega_\alpha t + \theta) \tag{3}$$

where $\varepsilon(z)$ denotes the spatial part of the electric field at $r = 0$,

$$E_z(r = 0) = \varepsilon(z) \cos(\omega_\alpha t + \theta) \tag{4}$$

and where a superscript prime denotes d/dz, ω_α is the angular frequency of the RF field, c is the speed of light in vacuum, and θ is the initial phase. Using longitudinal position z as the independent variable, the dynamics can be described in terms of canonical coordinates and momenta (x, p_x, y, p_y, t, p_t) and the new Hamiltonian is given by

$$H(x, p_x, y, p_y, t, p_t; z) \;=\; -\sqrt{p_t^2/c^2 - m^2c^2 - (p_x - qA_x)^2 - (p_y - qA_y)^2} - qA_z \tag{5}$$

where t denotes the particle's arrival time at the location z, its canonically conjugate momentum p_t is the negative of the particle's total energy, and q is the charge of the particle. One can next define a set of canonical variables that are dimensionless deviations from a reference trajectory, $(x = p_x = y = p_y = 0, t_0(z), p_{t0}(z))$, and one can obtain the corresponding Hamiltonian for these new variables. Expanding the new Hamiltonian around the reference trajectory, the lowest order terms are quadratic, and they govern the linear dynamics. The linear transfer matrix corresponding to the quadratic Hamiltonian can furthermore be factored as [11]

$$\begin{pmatrix} \bar{x} \\ \bar{p}_x \end{pmatrix}^f = \begin{pmatrix} u^{-1/2} & 0 \\ -u^{1/2}\Delta & u^{1/2} \end{pmatrix}^f \begin{pmatrix} a_x & b_x \\ c_x & d_x \end{pmatrix}^f \begin{pmatrix} u^{1/2} & 0 \\ u^{1/2}\Delta & u^{-1/2} \end{pmatrix}^i \begin{pmatrix} \bar{x} \\ \bar{p}_x \end{pmatrix}^i \tag{6}$$

$$\begin{pmatrix} \bar{y} \\ \bar{p}_y \end{pmatrix}^f = \begin{pmatrix} u^{-1/2} & 0 \\ -u^{1/2}\Delta & u^{1/2} \end{pmatrix}^f \begin{pmatrix} a_y & b_y \\ c_y & d_y \end{pmatrix}^f \begin{pmatrix} u^{1/2} & 0 \\ u^{1/2}\Delta & u^{-1/2} \end{pmatrix}^i \begin{pmatrix} \bar{y} \\ \bar{p}_y \end{pmatrix}^i \tag{7}$$

$$\begin{pmatrix} \phi \\ \bar{p}_t \end{pmatrix}^f = \begin{pmatrix} u^{-3/2} & 0 \\ -\frac{3l}{2}(\frac{u'}{u})u^{3/2} & u^{3/2} \end{pmatrix}^f \begin{pmatrix} a_\phi & b_\phi \\ c_\phi & d_\phi \end{pmatrix}^f \begin{pmatrix} u^{3/2} & 0 \\ \frac{3l}{2}(\frac{u'}{u})u^{3/2} & u^{-3/2} \end{pmatrix}^i \begin{pmatrix} \phi \\ \bar{p}_t \end{pmatrix}^i \tag{8}$$

where

$$\bar{x} = x/l, \quad \bar{p}_x = p_x/(mc) \tag{9}$$

$$\bar{y} = y/l, \quad \bar{p}_y = p_y/(mc) \tag{10}$$

$$\phi = \omega t - \omega t_0, \quad \bar{p}_t = (p_t - p_{t0})/(mc^2) \tag{11}$$

where $l = c/\omega$, ω is the scaling angular frequency, m is the rest mass of a particle, and superscripts i and f denote initial and final values, respectively. In the preceding formulas, Δ is given by

$$\Delta \;=\; \frac{l}{2}[\frac{(\beta_0\gamma_0)'}{\beta_0\gamma_0} - \frac{(q/mc^2)\varepsilon' \sin(\phi_s)}{\beta_0\gamma_0\omega_\alpha/c}] \tag{12}$$

and $u = \gamma_0\beta_0$, $l = c/\omega$, $\beta_0 = v_{z0}/c$, $\gamma_0 = 1/\sqrt{1-\beta_0^2}$, v_{z0} is velocity of the reference particle on axis, and ϕ_s is the synchronous phase of the reference particle given by $\phi_s = \omega_\alpha t_0(z) + \theta$. Here,

the time of flight t_0 and the relativistic factor γ_0 of the reference particle are given by

$$t_0' = \frac{\gamma_0/c}{\sqrt{\gamma_0^2-1}} \tag{13}$$

$$\gamma_0' = (q/mc^2)\varepsilon(z)\cos(\omega_\alpha t_0+\theta) \tag{14}$$

The quantities a_j, b_j, c_j, and d_j $(j = x, y, \phi)$ satisfy the following equations:

$$a_j' = c_j/l, \quad b_j' = d_j/l, \tag{15}$$

$$c_j' = -l\Omega_j a_j, \quad d_j' = -l\Omega_j b_j \tag{16}$$

with initial values $a_j = d_j = 1, b_j = c_j = 0$, and Ω_j $(j = x, y, \phi)$ are given by

$$\Omega_x = \Omega_y = \frac{(q/mc^2)(\omega_\alpha/c)}{2\beta_0^3\gamma_0^3}\varepsilon\sin(\phi_s) + \frac{1}{2}(1+\frac{\gamma_0^2}{2})(\frac{(q/mc^2)\varepsilon\cos(\phi_s)}{\beta_0^2\gamma_0^2})^2 \tag{17}$$

$$\Omega_\phi = \frac{\beta_0^2+\frac{1}{2}}{\beta_0^3\gamma_0}(q/mc^2)(\omega_\alpha/c)\varepsilon\sin(\phi_s) - \frac{3}{2}\frac{q/mc^2}{\beta_0^2\gamma_0}\varepsilon'\cos(\phi_s) + \frac{3}{2}(1-\frac{\gamma_0^2}{2})(\frac{(q/mc^2)\varepsilon\cos(\phi_s)}{\beta_0^2\gamma_0^2})^2 \tag{18}$$

As a test example, we transport a test particle through an RF cavity using the above linear transfer map and compare it with direct numerical integration of the Hamiltonian equations of motion. The computed trajectories from both methods are shown in Figure 2. The transfer map method agrees well with direct numerical integration in this example. Using above transfer maps for a single reference particle, we slice the beam longitudinally into multiple slices so that each slice has an individual reference particle through the RF cavity. The particle coordinates are converted into the multiple reference particle system coordinates in front of the RF cavity, tracking through the RF cavity, and then converted back to the original coordinates. Using a multiple reference particle helps capture the effect of nonlinear RF acceleration.

B. Treatment of Space Charge

The 3D space-charge forces are calculated at each time step from the solution of the Poisson equation in the beam frame using a convolution of the electron charge density with the Green function for the scalar potential with open boundary conditions. This convolution is calculated numerically on a 3D grid using an integrated Green function method with an FFT-based calculation of the cyclic summation on a doubled computational domain [12]. The space-charge fields are Lorentz transformed back to the laboratory frame and used along with the corresponding azimuthal magnetic self-field to advance the particle momentum.

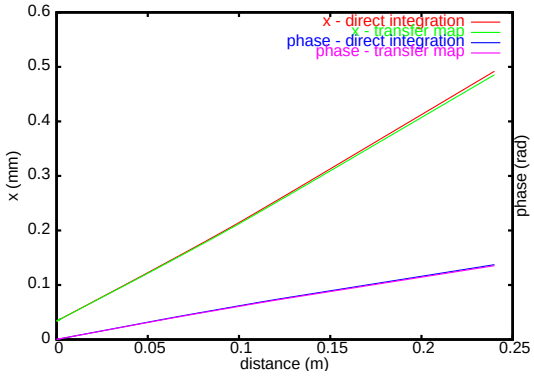

FIG. 2: Horizontal and longitudinal trajectories through an RF cavity from the linear transfer map and from direct numerical integration.

As a test of the space-charge model, we computed the energy modulation of an initial 120 MeV round uniform electron beam with $r_b = 200\mu$m radius and $I = 120$ A uniform current perturbed by a $A = 5\%$ modulation, and zero initial emittance propagating through three-meter drift space. Figure 3 shows the amplitude of energy modulation as a function of distance in comparison with an often used analytical model of longitudinal space-charge impedance [5]

$$Z(k) = \frac{iZ_0}{\pi\gamma_* r_b}\frac{1-\xi K_1(\xi)}{\xi}\bigg|_{\xi=kr_b/\gamma}, \tag{19}$$

where K_1 is the modified Bessel function, γ the relativistic factor, and $k = 2\pi/\lambda$ the wavenumber. This analytical model presupposes that the longitudinal component of the electric field across the beam is uniform and equal to the value on the beam axis. This is a good approximation if the wavelength of the perturbation as measured in the beam comoving frame is large compared to the beam transverse radius (*i.e.* $kr_b/\gamma \ll 1$). The relative energy modulation induced over the distance s by the model impedance (19) starting from a relative current sinusoidal modulation A is obtained from the formula $\Delta E/E = 4\pi A\frac{|Z(k)|}{Z_0}(sI)/(\gamma I_A)$, where $Z_0 \simeq 120\pi$ is the vacuum impedance and $I_A \simeq 17$kA the Alfvén current. However, as shown in the figure at smaller wavelengths this analytical model (dashed lines) tends to overestimate the energy modulation when this is averaged over the beam transverse density [13]. Indeed, a better approximation of the numerical result (see solid lines in the figure) is given by the average $Z_{\rm avg}(k) = \int_0^{r_b} Z(k) r dr/r_b^2$ yielding

$$Z_{\rm avg}(k) = \frac{iZ_0}{\pi\gamma_* r_b}\frac{1-2I_1(\xi)K_1(\xi)}{\xi}\bigg|_{\xi=kr_b/\gamma}. \tag{20}$$

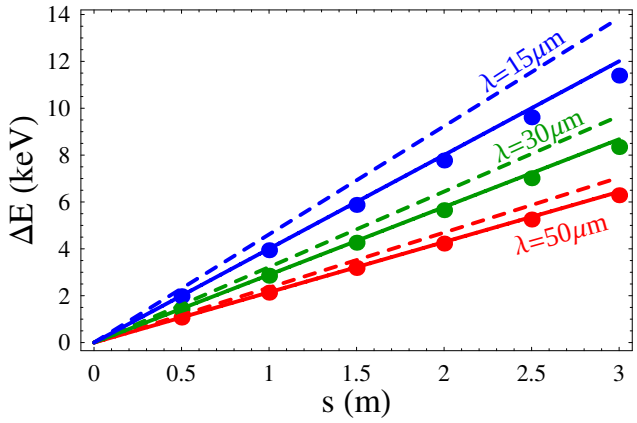

FIG. 3: Amplitude of energy modulations as a function of distance induced by space-charge starting from initial 5% current sinusoidal modulations with wavelengths $\lambda = 15\mu$m, 30μm and 50μm for a bunch with uniform transverse density and circular cross-section. The dots are from IMPACT simulations. The lines from the models of the longitudinal space-charge impedance discussed in the text.

C. Computation of Wakefields

The CSR is modeled as a one-dimensional (1D) longitudinal wake field as described in Ref. [14–16], where the change of energy due to CSR is given for steady state radiation by:

$$\frac{dE}{cdt} = -\frac{2e^2}{4\pi\epsilon_0 3^{1/3} R^{2/3}} \int_{-\infty}^{s} \frac{1}{(s-s')^{1/3}} \frac{d\lambda(s')}{ds'} ds' \tag{21}$$

To calculate above integral numerically, we carry out explicit low-pass filtering of the charge density and utilize a low order trapezoidal rule numerical integration scheme to $s - h$ [17]. Here, h is the mesh size for numerical integration. For explicit denoising we use filters that come with transfer functions uniformly approaching zero for frequency close to the Nyquist frequency and which are designed to conserve total charge and guarantee the non-negativity of the resulting filtered distribution density. They also should be computationally inexpensive to apply. An example of a filter that satisfies the above criteria and that also performed well in our tests is given by

$$\lambda_i = \frac{1}{96} \left(7\ \lambda_{i-2} + 24\ \lambda_{i-1} + 34\ \lambda_i + 24\ \lambda_{i+1} + 7\ \lambda_{i+2}\right) \tag{22}$$

Within the last mesh spacing, h, of the singularity we replace $\lambda(s)$ with a second-order polynomial fit to the smoothed density, and then evaluate the integral over $[s-h, s]$ analytically. Figure 4 shows the results of testing the CSR routine by simulation of the passage through a single 50 cm bend magnet of a distribution composed of 2 million particles all having equal energy, but with a sinusoidal charge density modulation in the z-direction. The modulation wavelength is 20 microns

with 20% amplitude. The beam has 0.8 nC charge with 230 MeV energy. The bunch length is 0.2 mm and the bending radius is 7.11 m. The solid blue line is the theoretical prediction, seen to be in very good agreement with the numerical simulation result, shown in red. It was confirmed in separate tests that the local energy spread in the final distribution is due to non-zero transverse emittance (0.015 mm-mrad) of the initial distribution. What appears to be a solid horizontal line at $\Delta\gamma = 0$ is an initial distribution footprint in the longitudinal phase space.

Besides the CSR wake field, the short range longitudinal wake field (monopole) and transverse wake field (dipole) are also included in the computational model of the IMPACT code. The effective forces from wake fields are given by:

$$F_x(s) = q\int_s^{\infty} W_T(s-s')x(s')\lambda(s')ds' \tag{23}$$

$$F_z(s) = q\int_s^{\infty} W_L(s-s')\lambda(s')ds' \tag{24}$$

where W_T is the transverse wake function, W_L is the longitudinal wake function, and λ is the line density function of the beam. For the effective force in the transverse y direction, x is replaced by y in Eq. 23. The transverse and longitudinal wake functions are provided externally according to different accelerating structures. To compute the effective forces from wake fields more efficiently, we extend the above integrals into a full domain convolution as:

$$F(s) = \int_{-\infty}^{+\infty} G(s-s')\rho(s')ds' \tag{25}$$

where

$$G(s) = \begin{cases} W_{T/L}(s) & for\ s \geq 0 \\ 0 & for\ s < 0 \end{cases} \tag{26}$$

$$\rho(s) = \begin{cases} x(s)\lambda(s) & for\ \ transverse\ wake \\ \lambda(s) & for\ \ longitudinal\ wake \end{cases} \tag{27}$$

The above convolution can be calculated using the same FFT-based method on a doubled computational domain as the space-charge force calculation. Figure 5 shows a comparison of the computational operations required to calculate the effective wake forces from the direct summation and from the FFT-based method. It is seen that after around 200 grid points, the FFT-based method is more efficient than the direct summation. Here, the doubled computational grid is included in the calculation of the number of operations for the FFT-based method.

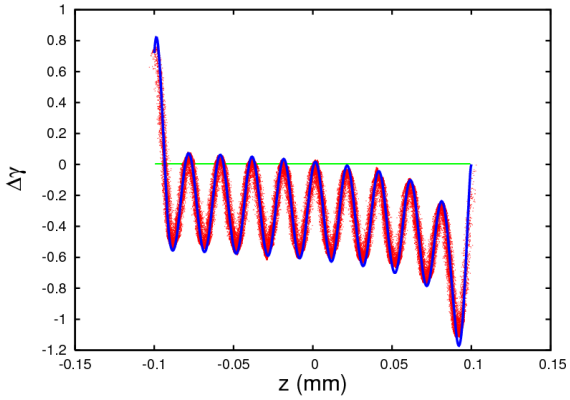

FIG. 4: Longitudinal phase space distribution after a bending magnet for an initial sinusoidal density modulation. Numerical result (red), analytical prediction (blue), and the initial distribution (green) are shown.

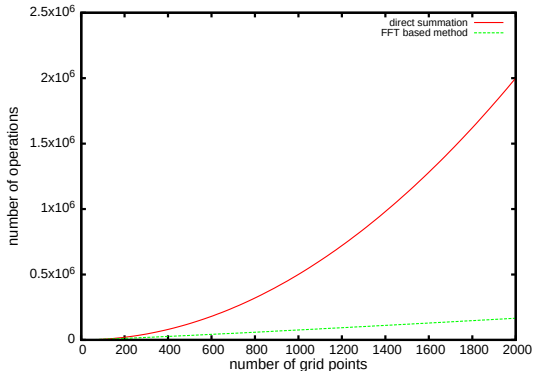

FIG. 5: Computational operations required for the effective wake force calculation as a function of grid number using direct summation and using the FFT method.

D. Macroparticle Up-Sampling of Initial Distribution

The FEL linac simulation starts with an initial electron beam coming out of a photoinjector. In most cases, this initial macroparticle distribution is produced by some other photoinjector simulation code. The number of macroparticles in the initial distribution can be as small as a few hundred thousand or a few million. For an electron beam with about 1 nC charge, this small number of macroparticles will cause significantly larger numerical shot noise [18]. In order to reduce the numerical noise in the initial macroparticle distribution, a much larger number of macroparticles, e.g. one billion macroparticles, are used to resample the original particle distribution (this process is also called up-sampling). In this study, a six-dimensional box centered at the original particle phase space location is used to up-sample the initial distribution. A uniform distribution is assumed inside the four-dimensional transverse phase space. Within the box, a linear current density distribution

is assumed based on the current profile from the original particle distribution. The correlated normalized energy deviation with the phase is obtained from the original distribution using a cubic spline. The normalized energy deviation $\bar{p}_t^{new}$ of each new particle inside the box is given by

$$\bar{p}_t^{new} = \bar{p}_t^{corr} + \delta p_t + \delta E \tag{28}$$

where $\bar{p}_t^{corr}$ is the correlated energy deviation in the original distribution, δp_t is the uncorrelated energy deviation in the original distribution, and δE is a new uncorrelated energy deviation generated from the sampling of a Gaussian distribution. Using the δE term helps emulate the effects of laser heater in the simulation. The box size of the up-sampling is controlled by the code user and should be chosen to produce sufficient smoothness of the resulting particle distribution while maintaining similar global properties (e.g. current profile) of the original distribution. Figure 6 shows the initial current profile of a Gaussian distribution from direct one billion macroparticle sampling and from one billion macroparticle up-sampling of a two million Gaussian particle distribution. It is seen that the results from direct sampling and from the up-sampling described above are in good agreement. Figure 7 shows the final longitudinal phase space using direct sampling and up-sampling in a beam dynamics simulation of the LBNL FEL linac. Again, the up-sampling scheme described here gives a good reproduction of the direct sampling result.

III. CHOICE OF NUMERICAL PARAMETERS

The choice of numerical parameters in the macroparticle beam dynamics simulation of an FEL electron linac can significantly affect the final results due to the fact that the microbunching instability is highly sensitive to initial noise level. Figure 8 shows the final slice averaged uncorrelated energy spread at the end of the linac studied at LBNL as a function of the number of macroparticles used in the simulation with an initial 5 keV and 2 keV uncorrelated energy spread for an electron beam charge of 0.8 nC. It is seen that the final slice averaged uncorrelated energy spread starts to saturate beyond 100 million macroparticles for 5 keV initial uncorrelated energy spread case, but continues to decrease for 2 keV case, where the microbunching instability is strong. Using a smaller number of macroparticles will lead to an unphysically larger energy spread. For 2 keV initial uncorrelated energy spread, the final slice averaged uncorrelated energy has a value close or less than that for the initial 5 keV case. This is due to the large oscillation of the slice uncorrelated energy spread across the bunch as shown by the larger error bars in the figure.

The performance of FEL radiation depends not only on uncorrelated energy spread but also on the energy fluctuation from slice to slice. Typical outcome of the microbunching instability is

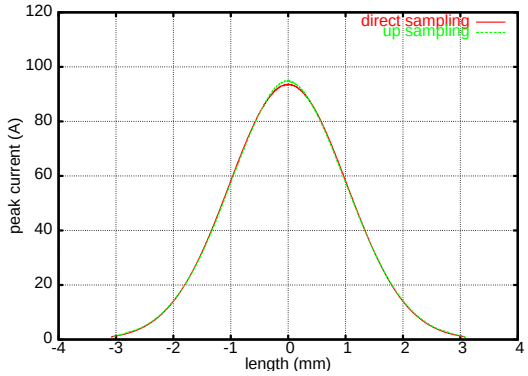

FIG. 6: Initial current distribution from direct sampling (one billion macroparticles) and up sampling (two million macroparticles).

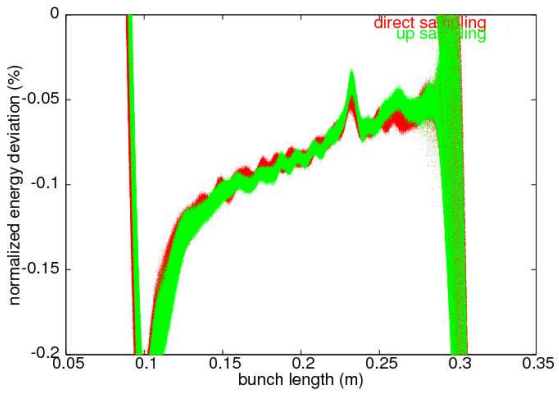

FIG. 7: Longitudinal phase space distribution at the end of the LBNL FEL linac from direct sampling and up sampling.

the fragmentation of the electron bunch longitudinal phase space into the large number of clusters of electrons centered at various energies. We note that the energy spread of the electrons in each cluster may not necessarily be large, but medium electron energy in the cluster may have a rather large offset from the nominal beam energy sometimes exceeding the rms energy spread by a large factor. Such electron bunch used for a generation of the x-ray pulses in the seeded free electron laser will produce the x-ray signal with significantly increased bandwidth compared to the electron bunch without clusters [19]. Figure 9 shows the final rms energy fluctuation as a function of the number of macroparticles used in the simulation. For the initial 5 keV uncorrelated energy spread case, the rms energy fluctuation approaches saturation of about 120 keV with macroparticle number beyond 1. For the initial 2 keV uncorrelated energy spread, the rms energy fluctuation keeps on decreasing till 5 billion macroparticles that is close to the real number of electrons for the 0.8 nC electron beam.

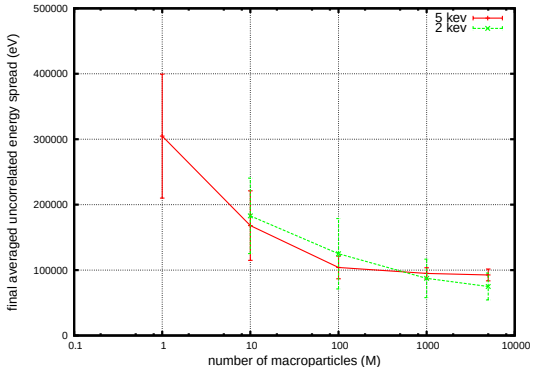

FIG. 8: Final slice averaged uncorrelated energy spread as a function of the number of macroparticles with initial 5 keV and 2 keV uncorrelated energy spread.

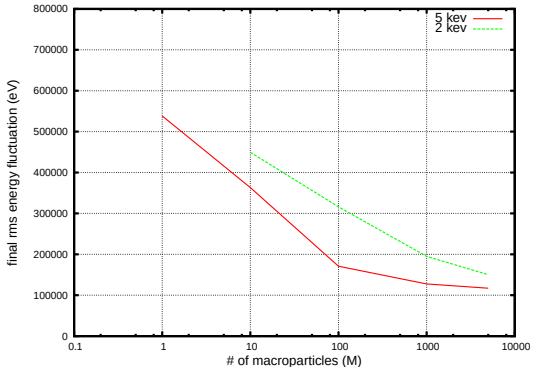

FIG. 9: Final electron beam rms energy fluctuation as a function of the number of macroparticles with initial 5 keV and 2 keV uncorrelated energy spread.

As the number of macroparticles approaches the real number of electrons in a bunch, the finite number of numerical grid points being used may present some unphysical smoothness of the electron beam density. This may numerically suppress some real shot noise in a bunch and result in less growth of the microbunching instability. Figure 10 shows the power spectrum of an initial current profile using 1024, 2048, 4096, and 8192 numerical grid points. For 1024 grid points, the maximum spatial frequency that can be resolved is about $0.17\mu m^{-1}$, i.e. 6μ m in wavelength. Any noise with a wavelength below 6μm will be suppressed by the grid. Using a larger number of grid points pushes the limit of resolution to higher frequency and smaller wavelength. However, the current noise level near low frequency ($< 0.1\mu m^{-1}$) or long wavelength ($> 10\mu m$) does not change significantly with the number of grid points beyond 2048. Increasing the number of grid points will mostly increase the initial current noise level at high frequency. On the other hand, the gain of the microbunching instability as a function of initial fluctuation wavelength can be calculated using a linear theory for a given linac lattice design. Figure 11 shows the gain function of the microbunching instability in

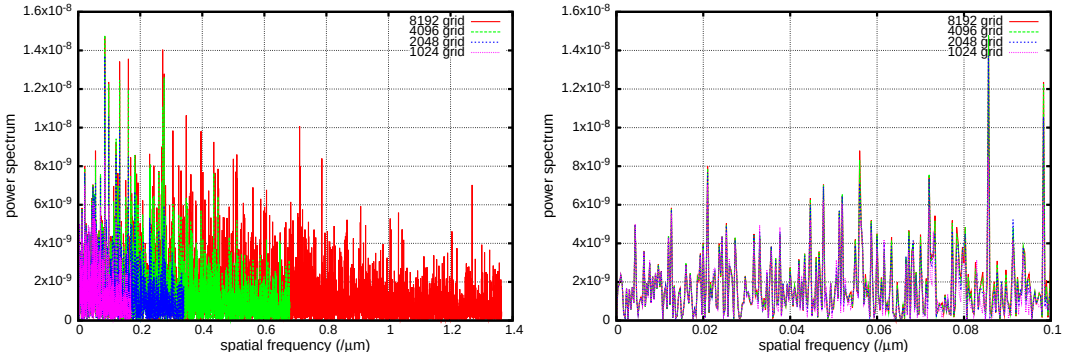

FIG. 10: Power spectra of the initial current profile using 1024, 2048, 4096, and 8192 grid points (left) and a zoom-in of the region of low spatial frequency (right).

the LBNL FEL linac design using the linear theory. It is seen that the gain of the microbunching instability decreases quickly at high frequency and has a peak near a low frequency around 260 um. Further increasing the number of grid points beyond 2048 will not change the initial shot noise level in the current profile near low frequency where the gain curve is peaked, and hence the final energy spread driven by the microbunching instability. To verify this hypothesis, we also carried out self-consistent one-billion macroparticle simulations of electron transport through the linac using two sets of numerical grid points. Figure 12 shows the final uncorrelated energy spread with 2048 and 4096 grid points. It is seen that both sets of grid points give nearly the same final energy spread. The above numerical example used an initial 5 keV uncorrelated energy spread. For a lower initial uncorrelated energy spread, the peak of the microbunching instability gain could move towards shorter wavelength, i.e. higher frequency. In this case, a larger number of numerical grid points would be needed to resolve the shorter wavelength in order to capture the physics of the microbunching instability.

IV. HIGH RESOLUTION SIMULATION OF A PLANNED FEL LINAC AT LBNL

A design effort is now underway for a planned soft X-ray FEL array at LBNL. We have carried out self-consistent macroparticle tracking of the driver linac using the IMPACT code with one billion macroparticles. Figure 13 shows a schematic plot of the linac [20]. It consists of a laser heater, two superconducting RF accelerating linac sections, a longitudinal phase space linearizer, a bunch compressor, and a spreader. The accelerating structure used in this study is based on a 1.3 GHz 9-cell superconducting RF cavity since this linac is designed for 1 MHz electron beam repetition rate. The energy of the electron beam at the entrance to linac is about 40 MeV. The

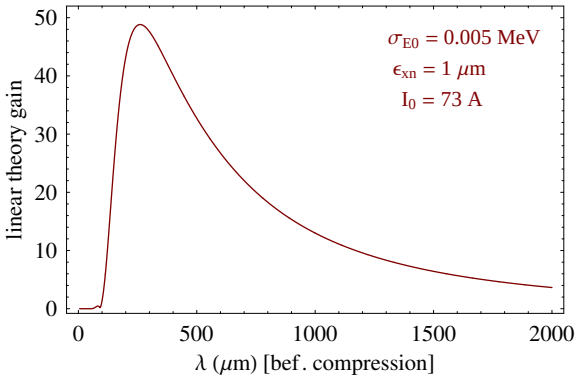

FIG. 11: The gain of microbunching instability in the LBNL FEL linac design as a function of noise wavelength from the linear theory.

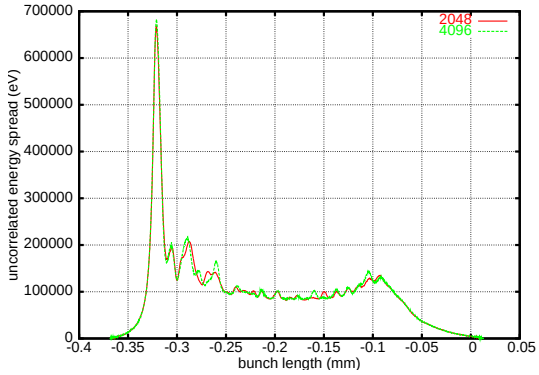

FIG. 12: Final energy spread from simulations using 2048 and 4096 grid points.

initial peak current is about 70 A with a total charge of 0.8 nC. The electron beam is accelerated to 250 MeV energy before entering the bunch compressor. A 3rd harmonic 3.9 GHz superconducting RF cavity is used as a longitudinal phase space linearizer in front of the bunch compressor. A single chicane bunch compressor is used in this design. Previous studies of the FERMI@ELETTRA FEL linac suggested that a single chicane could give a smaller final uncorrelated energy spread than the double chicane design [7, 21, 22]. After the bunch compressor, the electron beam is accelerated to a final energy of 2.4 GeV with a peak current near 1.2 kA.

Studies conducted for the FERMI@ELETTRA FEL design suggested that there could be an optimal initial current profile for producing the desired beam quality at the end of the linac [23]. Given the same rms bunch length and similar peak current, the detailed shape of the initial current profile can have significant impact on final beam quality. Figure 14 shows the final energy spread for four different initial current distributions. Here, LiTrack 1 and LiTrack 2 denote two initial current distributions obtained from back tracking an ideal current profile from the end of the linac using the Litrack code. The parabolic distribution with the same rms bunch length produces the

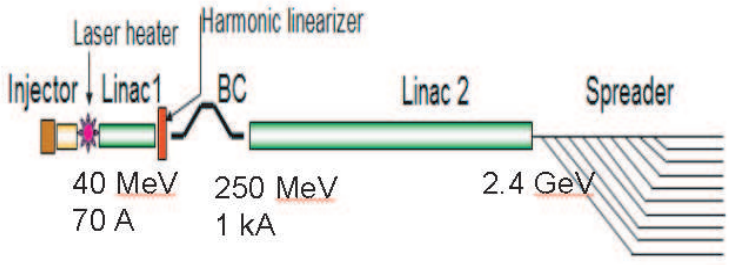

FIG. 13: A schematic plot of a planned FEL linac at Berkeley.

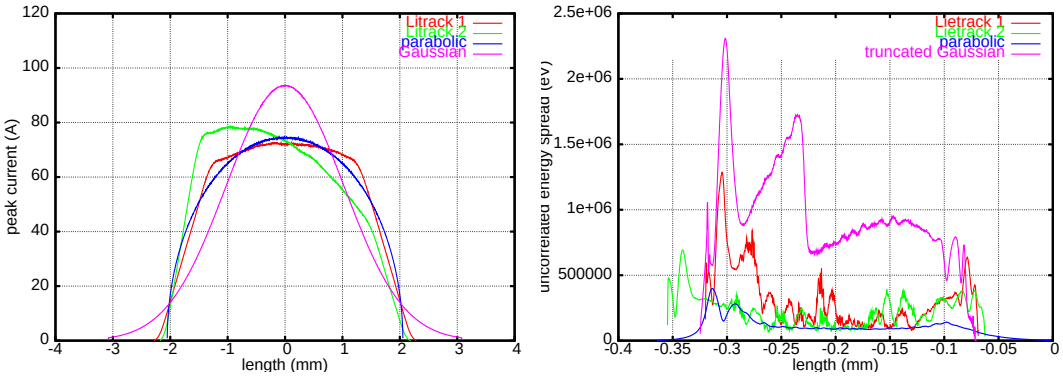

FIG. 14: Four types of initial current profiles (left) and the final uncorrelated energy spread corresponding to these initial profiles (right).

lowest energy spread at the end of the linac. The large uncorrelated energy spread from the initial Gaussian distribution is due to the longitudinal phase space bifurcation at the end of the linac as shown in Figure 15.

The uncorrelated energy spread in an electron beam can smear out coherent growth of the microbunching instability. A larger initial energy spread leads to less growth of the microbunching instability. Figure 16 shows the final uncorrelated rms energy spread along the bunch length for 6 different values of initial uncorrelated energy spread. It is seen that for 2 keV initial energy spread, there exist large amplitude short wavelength fluctuations driven by the microbunching instability. For 5 keV initial uncorrelated energy spread, the fluctuations become much smaller and move towards longer wavelength. Throughout most of the bunch, beyond 5 keV initial energy spread, the final energy spread shows a linear dependence on the initial energy spread due to the bunch compression. The microbunching instability has been sufficiently suppressed by the incoherent motion of electrons with large initial energy spread.

Figure 17 shows the longitudinal phase space distribution at the end of the linac from a simulation using an initial parabolic current profile, 5 keV uncorrelated energy spread, and 0.75 mm-mrad

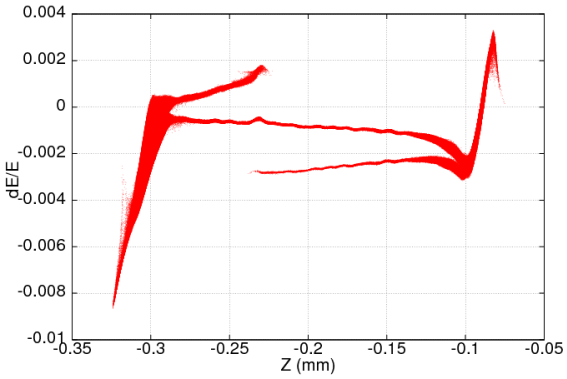

FIG. 15: Final longitudinal phase space from the initial Gaussian current distribution.

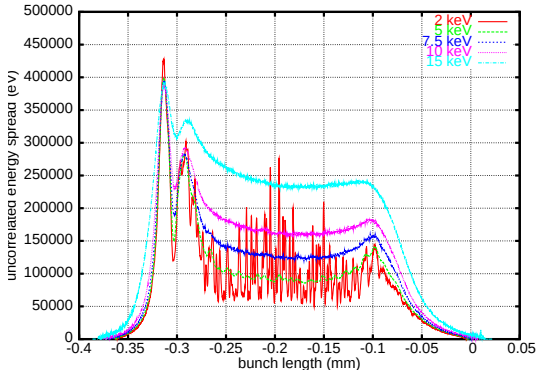

FIG. 16: Final uncorrelated energy spread distribution resulting from an initial parabolic current profile with initial 2 keV, 5 keV, 7.5 keV, 10 keV and 15 keV uncorrelated energy.

transverse emittance. It is seen that the full width of the final relative energy spread is on the order 10^{-4} for a major part of beam (the rms relative energy spread is 10^{-5}). Such a small energy spread will be especially important for cost effective seeded FEL applications. There is small energy modulation in the longitudinal phase space with a period of around 15 um. After accounting for a compression factor of 17, this modulation period is in a good agreement with the gain function of the microbunching instability shown in Figure 11 from the linear theory. This modulation comes from the initial shot noise in a 0.8 nC beam sampled with one billion macroparticles, and is further amplified through the linac due to the microbunching instability.

Figure 18 shows the current profile at the end of the linac. The peak of the current profile reaches about 1.2 kA with a reasonably flat distribution along a major part of the beam.

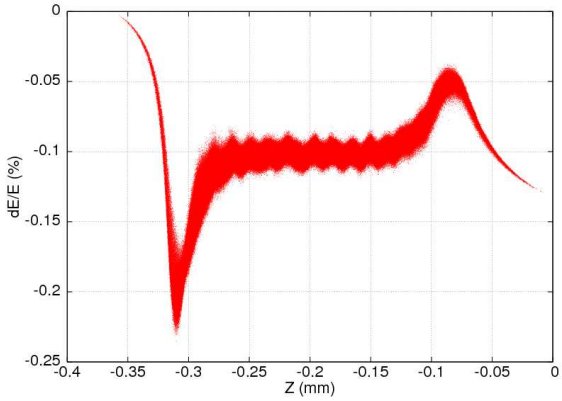

FIG. 17: Longitudinal phase space at the end of the linac with initial 5 keV rms uncorrelated energy spread.

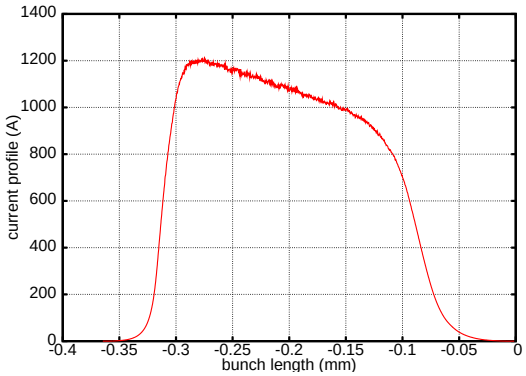

FIG. 18: Current profile at the end of the linac with initial 5 keV rms uncorrelated energy spread.

V. SUMMARY AND DISCUSSIONS

In this study we have shown that large scale, multi-physics simulation is needed to accurately model electron beam transport in the presence of the microbunching instability when designing a linac for future FEL applications. We have presented the latest developments of the IMPACT code that have made large scale macroparticle simulation possible. Up-sampling based on local particle phase-space location and global energy-phase correlation results in good reproduction of direct large-number macroparticle sampling. Numerical parameters such as number of macroparticles and number of computational grid points need to be chosen carefully to simulate initial shot noise in the electron bunch and to capture the detailed physics of the microbunching instability. As an application, we performed simulations with one billion macroparticles of electron beam transport through a linac designed to drive an array of soft X-ray FELs at LBNL. We observed that the initial current profile shape affects the final uncorrelated energy spread of the beam. Among different initial current profiles used in this study, the parabolic current distribution produced the lowest

uncorrelated energy spread at the end linac, around 100 keV. The effects of initial uncorrelated energy spread were also studied. Using 5 keV initial energy spread resulted in the lowest level of energy spread at the end of the linac.

The microbunching instability is primarily driven by longitudinal space charge that is responsible for the growth of the uncorrelated energy spread at the end of the linac [5]. In this study, we focused on the longitudinal space-charge effect and turned off the transverse space-charge effects inside the code. Including the transverse space-charge effects led to rms mismatch near the entrance of the linac and more than 30% emittance growth. Optimization of the linac lattice design including 3D space-charge effects is still in progress and will be reported in another publication. At present, one billion macroparticle beam dynamics simulations of the planned FEL linac at LBNL have already shown that a reasonable beam quality can be achieved at the end of the linac with about 100 keV energy spread at 2.4 GeV energy, and 1.2 kA peak current.

ACKNOWLEDGMENTS

We would like to thank Drs. W. Fawley and G. Penn for discussions. This research was supported by the Office of Science of the U.S. Department of Energy under Contract No. DE-AC02-05CH11231. This research used resources of the National Energy Research Scientific Computing Center.

REFERENCES

[1] E. L. Saldin, E. A. Schneidmiller, and M. V. Yurkov, Nucl. Instrum. Methods Phys. Res., Sect. A **483**, 516 (2002).

[2] M. Borland *et al.*, Nucl. Instrum. Methods Phys. Res., Sect. A **483**, 268 (2002).

[3] S. Heifets, G. Stupakov, S. Krinsky, Phys. Rev. ST Accel. Beams, vol 5, 064401 (2002).

[4] Z. Huang, M. Borland, P. Emma, K. Kim, Nucl. Instrum. Methods Phys. Res., Sect. A **507**, 318 (2003).

[5] Z. Huang, M. Borland, P. Emma, J. Wu, C. Limborg, G. Stupakov, J. Welch, Phys. Rev. ST Accel. Beams, vol 7, 074401 (2004).

[6] M. Borland, Phys. Rev. ST Accel. Beams, vol 11, 030701 (2008).

[7] M. Venturini, Phys. Rev. ST Accel. Beams, vol 10, 104401 (2007).

[8] C. Bocchetta, *et al.* "FERMI@WLETTRA: A seeded harmonic cascade FEL for EUV and soft x-rays," SLAC-PUB-11488, September 2005.

[9] J. Qiang, R. Ryne, S. Habib, V. Decyk, J. Comp. Phys. vol. 163, 434, (2000).

[10] R. D. Ryne, J. Qiang, and S. Habib, in *The Physics of High Brightness Beams*, ed. by J. Rosenzweig and L. Serafini, p. 91, World Scientific, 2000.

[11] R. D. Ryne, "The linear map for an RF gap including acceleration," Los Alamos National Laboratory Tech. Report, 1995.

[12] J. Qiang, S. Lidia, R. D. Ryne, and C. Limborg-Deprey, Phys. Rev. ST Accel. Beams, vol 9, 044204 (2006).

[13] M. Venturini, Phys. Rev. ST Accel. Beams, vol 11, 034401 (2008).

[14] E. L. Saldin, E. A. Schneidmiller, and M. V. Yurkov, Nucl. Instrum. Methods Phys. Res., Sect. A398, 373 (1997).

[15] M. Borland, Phys. Rev. Special Topics - Accel. Beams 4, 070701 (2001).

[16] G. Stupakov and P. Emma, "CSR wake for a short magnet in ultrarelativistic Limit," SLAC-PUB-9242, 2002.

[17] I. Pogorelov, et. al., Proc. ICAP 2006, Chamonix, France, 182 (2006).

[18] L. Giannessi, Phys. Rev. Special Topics - Accel. Beams 6, 114802 (2003).

[19] L. Yu, Phys. Rev. A 44, 5178 (1991).

[20] A.A. Zholents, E. Kur, G. Penn, J. Qiang, M. Venturini, R. P. Wells, "Linac design for an array of soft x-ray free electron lasers", to be published in Proc. of Linac conference, 2009, Victoria, Canada.

[21] J. Qiang, "One billion macroparticle simulation of microbunching instability at Fermi FEL linac using the IMPACT code," in Workshop on the Microbunching Instability, Sep. 17-19, Elettra Laboratory at Sincrotrne Trieste, Italy, 2007.

[22] M. Cornacchia, *et al.*, "Running fermi with one-stage compressor: advantages, layout, performance," LBNL-62765, 2008.

[23] M. Cornacchia, S. Di Mitri, G. Penco, and A. A. Zholents, Phys. Rev. Special Topics - Accel. Beams 9, 120701 (2006).